Applied Magnetic Resonance (2022) 53:1175–1193
https://doi.org/10.1007/s00723-021-01438-8

Applied
Magnetic Resonance

ORIGINAL PAPER

D-Band EPR and ENDOR Spectroscopy of ^{15}N-Labeled Photosystem I

Jens Niklas[1] · **Udita Brahmachari**[1] · **Lisa M. Utschig**[1] · **Oleg G. Poluektov**[1]

Received: 4 June 2021 / Revised: 29 September 2021 / Accepted: 3 October 2021 /
Published online: 20 November 2021

Abstract

For billions of years, nature has optimized the photosynthetic machinery that converts light energy into chemical energy. Key primary reactions of photosynthesis occur in large membrane protein–cofactor complexes. The light-induced sequential electron transfer reactions occur through a chain of donor/acceptor cofactors embedded in the protein matrix resulting in a long-lived transmembrane charge-separated state. EPR is the method of choice to study electron transfer and the interaction of protein environment with redox-active cofactors. However, the spectra of organic cofactor radicals typically are not fully resolved and severely overlap at conventional X-band EPR. Even at Q-band EPR, this overlap is present and often a serious problem. As a result, there is a large variation of the reported EPR data and limited understanding of electronic structures of several redox-active cofactors. These serious problems can often be overcome by the excellent spectral resolution provided by high-frequency EPR (HF EPR). Here, we study the electronic structure of the primary electron donor P_{700} and the secondary electron acceptor A_1 of Photosystem I (PSI) using 130 GHz (D-band) EPR and Electron–Nuclear-Double-Resonance (ENDOR) spectroscopy. PSI was isotopically labeled with ^{15}N ($I=½$) to avoid quadrupolar interactions in the most abundant nitrogen isotope ^{14}N ($I=1$) and simplify the ENDOR spectra. ENDOR spectroscopy is central for determining the hyperfine coupling of nitrogen atoms of the two chlorophyll molecules comprising oxidized P_{700} and the involvement of protein nitrogen atoms with reduced A_1. While HF ENDOR of A_1^- allows identification of two nitrogen atoms, HF ENDOR of P_{700}^+ still does not permit unique assignment of the recorded hyperfine couplings.

✉ Lisa M. Utschig
Utschig@anl.gov

✉ Oleg G. Poluektov
Oleg@anl.gov

[1] Chemical Sciences and Engineering Division, Argonne National Laboratory, 9700 S. Cass Ave., Lemont, IL 60439, USA

1 Introduction

Photosynthesis is the light-driven process used by plants and cyanobacteria to produce carbohydrates from carbon dioxide and water [1–3]. The oxygenic version of photosynthesis is the basis for all higher life on earth. The chemical reactions in photosynthesis can be divided into the light reactions and dark reactions. The early steps of the light reactions consist of a series of light-induced electron transfer (ET) reactions. The light reactions occur in photosynthetic reaction center (RC) proteins with near unity quantum efficiency, something not yet achieved in artificial systems [4]. Photosynthetic RCs are large, integral transmembrane protein–cofactor complexes in which light-initiated rapid, sequential electron transfers result in the formation of stabilized charge separation across the membrane, which is then used to drive subsequent chemical dark reactions of photosynthesis [1–3,5–7]. The ET events inside the RCs occur through a chain of electron donor and acceptor molecules. There are two types of photosynthetic RCs, Type I and Type II, as defined by their terminal electron acceptor cofactors. Type II RCs use quinones as their terminal electron acceptors, while Type I RCs use FeS clusters as terminal electron acceptors [1,8–14]. Photosystem I (PSI) of oxygenic photosynthesis is the most important representative of Type I RCs. X-ray analysis of PSI single crystals reveals two branches of cofactors, termed A and B, arranged in a pseudo two-fold symmetry (Fig. 1A) [8, 9]. Each branch contains three chlorophylls and one quinone as central cofactors involved in ET, while a large number of additional chlorophylls and carotenoids act as an internal light-harvesting antenna which, upon absorption of a photon, funnels the energy to the central chlorophyll cofactors. In the "standard model" of charge separation in PSI, in analogy with other photosynthetic RCs, light-induced electron transfer starts from the primary electron donor P_{700}, consisting of a pair of chlorophyll molecules (P_A and P_B, Fig. 1B), each from one branch. Alternatively, the very first step of charge separation might start from the second chlorophyll in either the A- or B-branch, so-called accessory chlorophylls. The "primary donor" P_{700} would then be oxidized only in the second step, reducing the oxidized accessory chlorophyll [15–18]. Independent of the location of the first ET step, the electron is transferred rapidly to the primary acceptor chlorophyll termed A_0, and then to the next electron acceptor termed A_1 (phylloquinone, VK_1). In contrast to Type II RCs, neither of the two quinone molecules in PSI, termed A_{1A} and A_{1B}, acts as terminal electron acceptor, but under physiological conditions sequential ET continues to three [4Fe–4S] clusters termed F_X, F_A, and F_B (Fig. 1A) [6, 19, 20]. The ET in PSI was presumed for a long time to be unidirectional (ET in only one of the two branches) by analogy to Type II RCs, like the purple bacterial RC, despite no different functionality of the quinones A_{1A} and A_{1B}. Now it is generally accepted that electron transfer can occur on both branches, though the exact "branching ratio" may depend on the species from which PSI is isolated as well as details of the biochemical procedures [6,20–27]. At low temperature, the ET behavior is somewhat different. ET along the A-branch is blocked at low temperature beyond A_{1A} quinone, while ET along the B-branch continues to the

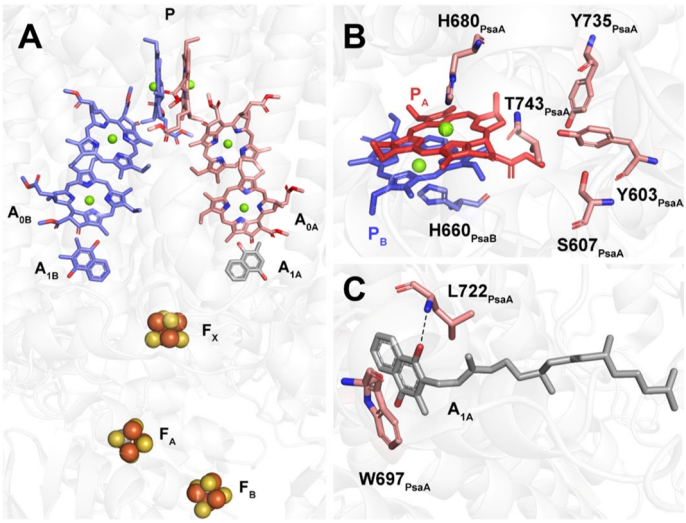

Fig. 1 **A** Scheme of cofactor arrangement and ET pathways in Photosystem I (PSI) RC. The cofactors are arranged in two symmetric branches, A (red) and B (blue). Following photoexcitation, the primary donor P_{700} becomes oxidized, transferring its electron to one of two identical chains of donor/acceptor molecules: chlorophyll A_0, phylloquinone A_1, and three [4Fe–4S] clusters, F_X, F_A, and F_B. **B** Structure of primary donor P_{700}, a dimer of Chlorophyll *a* (P_B) and a Chlorophyll *a*' (P_A) and selected surrounding amino acids. Both Chls are axially singly ligated by histidines ($H680_{PsaA}$ and $H660_{PsaB}$, respectively), and Chlorophyll *a*' is hydrogen bonded to threonine $T743_{PsaA}$. **C** Structure of secondary acceptor A_{1A}, vitamin K_1 (VK_1), and selected surrounding amino acids. Only one oxygen of VK_1 is involved in a hydrogen bond with a leucine ($L722_{PsaA}$). Structural coordinates from crystal structure of PSI from *T. elongatus* (PDB code 1JB0) (color figure online)

[4Fe–4S] clusters, generating a quite stable (long-lived) charge separated state P_{700}^+ $[F_A,F_B]^-$ in a certain fraction of PSI RCs [19,20,25–28]. At low temperature, [4Fe–4S] clusters act as deep traps for electrons and thus electron recombination to the oxidized primary donor P_{700}^+ is largely suppressed.

P_{700} has been extensively investigated over the years because of its important role in the redox chemistry of PSI, potentially directing the light-generated electron to the A- or B-branch [6]. However, gaps in knowledge still remain. X-ray crystallography [8,9] has shown the primary donor P_{700} is a Chl *a*/Chl *a'* heterodimer in which the two Chl molecules are in a coplanar arrangement (Fig. 1B). The two chlorin planes partially overlap (at rings I and II) and have an average interplanar distance of 3.6 Å. Both Chls are located on the sides of an approximate C_2 symmetry axis. In addition to the asymmetry in chemical composition, further asymmetry is imparted by the surrounding protein environment. While both Chls are symmetrically axially ligated by histidine residues to the central Mg ions ($H680_{PsaA}$ and $H660_{PsaB}$, respectively), only the A-site Chl *a'* is hydrogen bonded to the protein. The keto carbonyl oxygen (13^1) on ring E is H-bonded to Threonine ($T743_{PsaA}$) and the phytyl ester carbonyl oxygen is H-bonded to Tyrosine ($Y735_{PsaA}$). Furthermore, the carboxy oxygen of the 13^2-carbomethoxy

group is H-bonded by water. Several amino acids are also part of an H-bond network involving this water molecule ($Y603_{PsaA}$, $S607_{PsaA}$, $T743_{PsaA}$).

While many spectroscopic methods have been applied to study the primary donor P_{700}^+, electron paramagnetic resonance (EPR) techniques have been the most useful for gaining detailed insight about its electronic structure [29,30]. One of the main motivations of this research is a wide variety of the reported hyperfine couplings (hfc) of the nitrogen atoms in the literature. The EPR spectra of organic cofactor radicals typically severely overlap with unresolved canonical components at conventional EPR frequency of 9.5 GHz (X-band), limiting information about their electronic structure. This might be one of the sources for variation in the hfc data. These serious problems can be overcome by utilizing high-frequency EPR, which provides much higher spectral resolution [31–38]. Orientation-selective Electron-Nuclear-Double-Resonance spectroscopy (ENDOR) at D-band (130 GHz) allows more precise determination of unresolved hyperfine interactions with magnetic nuclei, thus providing further details about the electronic properties of protein-embedded cofactors. Here, we use D-band EPR and ENDOR spectroscopy to study the primary electron donor P_{700} and the secondary electron acceptor A_1 in PSI. The asymmetry of the spin density distribution in P_{700} has been extensively investigated using ENDOR spectroscopy to determine the hyperfine couplings of nitrogen atoms of the two chlorophylls comprising P_{700}. However, there is still no consensus on the interpretation and assignment of the nitrogen hyperfine coupling (hfc) data obtained by ENDOR and ESEEM/HYSCORE techniques. The secondary electron acceptor A_1 has a single H-bond to the protein via a peptide nitrogen atom (Fig. 1C). This interaction modulates electronic properties of A_1 which is essential for efficient ET. The reliable identification of nitrogen hfc at conventional X-band EPR/ESEEM/HYSCORE is obscured by spectral overlap with other organic species, like the anion radical of the primary acceptor Chl A_0, as well as substantial quadrupolar interactions related to the most abundant nitrogen isotope ^{14}N with a nuclear spin $I=1$. The unique availability of ^{15}N labeled photosynthetic microorganisms in our laboratory was further impetus for this study. To simplify interpretation of the ENDOR spectra, PSI was isotopically labeled with ^{15}N, which has $I=½$ and thus no quadrupolar interactions. Furthermore, PSI was also fully deuterated reducing the EPR linewidth and allowing resolution of the small electronic g-tensor anisotropy of P_{700}^+ at D-band. For the study of A_1^- a biochemical procedure has been used to generate a stable, stationary A_{1A} radical anion. In this procedure, the [4Fe–4S] clusters F_A and F_B are chemically reduced and reduction of F_X and A_1 is achieved by illumination of PSI samples at temperatures slightly above 200 K [20, 27, 28, 39–46]. 130 GHz EPR allowed both the resolution of the electronic g-tensor of A_1^- and also spectral separation of A_1^- from background signals and side products generated due to the chemical reduction and following photoaccumulation procedure.

2 Materials and Methods

2.1 Sample Preparation

Fully deuterated cyanobacteria were cultured from pure water to 99.6% D_2O by incremental increases in D_2O. This procedure gives time for the cyanobacteria to adapt to heavy water conditions. Once a healthy culture is successfully growing in fully deuterated conditions, this 50 ml culture is then used to inoculate 5 l of deuterated, ^{15}N media. Fully deuterated, fully ^{15}N-substituted *Synechococcus lividus* was grown at 48 °C under fluorescent lighting fixtures in closed Lucite rocking-box units containing 5 L of culture media as detailed in ref [47]. 4 g of $K^{15}NO_3$ (from Oak Ridge National Laboratory) was used per 1 L of media. Once optimal culture growth was achieved, the cyanobacteria were harvested and PSI reaction centers were isolated and purified as described in ref [48]. Purified PSI was prepared in 50 mM MES, pH 6.5, 20% glycerol, 0.03% β-DM (*n*-dodecyl β-D-maltopyranoside, Anatrace), and 30 mM sodium ascorbate. For EPR measurements on P_{700}^+, the PSI sample was concentrated to 150 μM PSI monomer with final conditions of 50 mM Tris–Cl, pH 8.3, 20% glycerol, 0.03% β-DM, and 10 mM sodium ascorbate. For EPR measurements of A_1^- and A_0^-, PSI samples were prepared in 50 mM glycine–KOH, pH 10, 20% glycerol, 0.03% β-DM and 40 mM sodium hydrosulfite. All samples were dark-adapted for ~ 15 min at room temperature. This procedure leads to the reduction of F_A and F_B iron–sulfur centers in the sodium hydrosulfite containing samples. The samples were loaded into quartz tubes (inner diameter 0.5 mm/outer diameter 0.6 mm), dark-adapted, and placed in the microwave cavity. The cavity was held in an Oxford flow cryostat, and temperature was controlled by the Oxford temperature control system. Sodium ascorbate containing samples for the measurement of P_{700}^+ were cooled down to 100 K from ambient temperature under illumination. Sodium hydrosulfite containing samples were cooled down to 205–210 K in the dark, followed by illumination for various time durations with 532 nm laser light. This combination of reduction with sodium hydrosulfite and illumination (referred in the following to as "photoaccumulation" procedure) results in the successive reduction of F_X and A_{1A} and A_{0A} [20, 27, 39, 40, 42–46].

2.2 EPR and ENDOR Spectroscopy

EPR measurements were performed on a pulsed/continuous wave high-frequency D-band (130 GHz/4.6 T) EPR spectrometer [33,49] with single mode cylindrical cavity TE_{011}. Pulsed EPR spectra were recorded by monitoring the electron spin echo (ESE) intensity from a two microwave (mw) pulse sequence as a function of magnetic field (FSE, Field-Swept-Echo detected EPR). The duration of the π/2 microwave pulse was 40–50 ns and separation times between microwave pulses were 200 ns. Pulsed Mims ENDOR spectra were recorded by monitoring the electron spin echo (ESE) intensity from a three microwave pulse sequence ($\pi/2-\tau-\pi/2-t-\pi/2-\tau-$echo) as a function of radiofrequency [50–53]. The duration

of the π/2 microwave pulses was 40–50 ns, separation times between the first two microwave pulses (τ) were varied in the range 150–500 ns, and *t* was 200 µs. A Rhode & Schwarz RF synthesizer and a BT01000-AlphaSA 1 kW RF amplifier (TOMCO Technologies, Stepney, Australia) were used to deliver an RF π-pulse of 120 µs between the second and third mw pulse. Light excitation of the sample was achieved with an optical parametric oscillator (OPO, GWU-Lasertechnik) pumped by a Nd:YAG laser (Quanta-Ray INDI, Spectra Physics), the output of which was coupled to an optical fiber. The optical fiber allows delivery of up to 2 mJ per pulse to the sample. Excitation wavelength was 532 nm. Data processing was undertaken using Matlab 2018b (MathWorks, Natick, US). Simulations of EPR and ENDOR spectra were performed using the Easyspin software (version 6.0.0) [54].

3 Results and Discussion

3.1 Electronic Structure of the Cation Radical of the Primary Donor P_{700}^+

The P_{700}^+ cation radical was generated by illumination at low temperature to avoid potential unwanted reactions that can occur with chemical oxidation. A typical field-swept echo detected EPR spectrum recorded at high-frequency D-band (130 GHz, 4.6 T) is shown in Fig. 2A. The spectrum was recorded in pulsed mode and shows an absorption type spectrum, not the more typical first-derivative type spectrum obtained with continuous wave (cw) EPR spectroscopy. The spectrum is due to a single unpaired electron spin, dominated by a slightly rhombic g-tensor and shows no resolved hyperfine structure. Note, that this spectrum demonstrates a reduction in line width as compared to the signal of P_{700}^+ in fully protonated and ^{14}N-containing PSI [29,30,33,36,55–59]. Simulation of the D-band EPR spectrum provided the principal g-tensor values of 2.00309 (g_x), 2.00263 (g_y), and 2.00225 (g_z), which are all very close to the *g* value of the free electron ($g_e \approx 2.00232$), indicating very weak spin–orbit coupling [60–62]. These values are in excellent agreement with previous high-frequency P_{700}^+ EPR studies of perdeuterated PSI, and frozen solution and single-crystal EPR studies of protonated PSI [29,30,33,36,55–59]. The arrows in Fig. 2A mark the magnetic field positions where the three Mims ENDOR spectra were recorded (Fig. 2B). These positions approximately correspond to the principal values of the g-tensor. The length of the π/2 mw pulses in the Mims ENDOR pulse sequence provides an excitation width of approximately 20 MHz, [53] which slightly exceeds the anisotropic broadening used to simulate the EPR spectrum (11–13 MHz). Thus, even for the two outer magnetic field positions the ENDOR spectra are not fully single-crystal type ENDOR spectra. An important consideration for analysis of the ENDOR spectra is the orientation of the electronic g-tensor within the molecular axes system of the cofactor radical. For a planar, delocalized organic π-type molecular radical like a Chl, two components of the g-tensor are expected to be in the plane, while the third one (with the lowest g value) is oriented perpendicular to the plane [60,61,63]. For the primary donor in PSI this is not the case. The g-tensor orientation of P_{700}^+ was determined by two independent EPR methods, and it was found that all three principal g-tensor axes deviate substantially

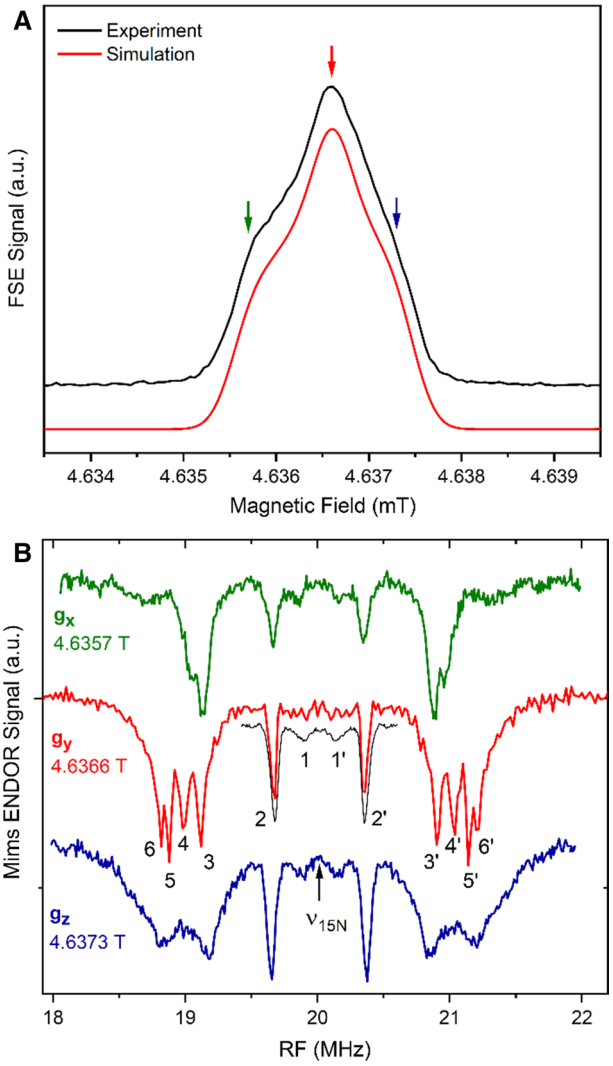

Fig. 2 High-frequency (130 GHz) pulsed EPR and ENDOR spectra of the P_{700}^{+} cation radical. All spectra were recorded at $T = 50$ K. **A** High-frequency (130 GHz, D-band) pulsed EPR spectrum of the P_{700}^{+} cation radical (black) and its simulation (red). Simulation parameters for the g-tensor: 2.00309, 2.00263, 2.00225. Colored arrows indicate the magnetic field positions where the ENDOR spectra were acquired. **B** ^{15}N Mims ENDOR spectra recorded at three magnetic field positions corresponding approximately to principal values of the electronic g-tensor. Note that Mims ENDOR signals are negative. Spectra were recorded with $\tau = 200$ ns, except narrow black spectrum, $\tau = 500$ ns (color figure online)

from the molecular axes system [29,30,58,59]. This complicates the determination of principal hyperfine coupling constants and the assignment of hyperfine tensors to specific nuclei. This also explains why ENDOR spectra recorded along g_x and g_z are relatively broad, while at the two outer canonical orientations, g_x and g_z, ENDOR spectra often exhibit quite narrow, single-crystal type lines.

The first-order resonance condition for ENDOR spectroscopy of ^{15}N nuclei is $\nu_{ENDOR} = |\nu_{15N} \pm A/2|$, where ν_{15N} is the Larmor frequency of a "free" ^{15}N nucleus and A is the hyperfine coupling [51–53,64]. For comparison of ^{15}N hyperfine couplings with those of the naturally occurring ^{14}N nucleus ($I = 1$, 99.6% abundance), the hyperfine couplings need to be scaled with ^{14}N/^{15}N gyromagnetic ratio of ≈1/1.40. Since all nitrogen hyperfine coupling constants are much smaller than the Larmor frequency at ≈4.636 T (^{15}N Larmor frequency ≈20.0 MHz), ENDOR signals of each nitrogen nucleus coupled to the unpaired electron spin manifest themselves as a line pair with a distance of A/2 from the ^{15}N Larmor frequency. ENDOR signals of other magnetic nuclei in P_{700}^+ are well-separated from ^{15}N signals due to the large Zeeman effect at these high magnetic fields. Since the Mims ENDOR sequence is based on the three pulse stimulated echo sequence, it suffers from so-called blindspots for a hfc $A = 1/\tau$ and a suppression of ENDOR signals close to the Larmor frequency [50–53]. The ENDOR spectra at g_X, g_Y, and g_Z positions, shown in Fig. 2B, were recorded with $\tau = 200$ ns, corresponding to the first blindspot for hyperfine couplings of 5 MHz, which is outside of the range acquired. In order to check that there are no hfcs larger than 5 MHz, several spectra were recorded at different τ-values in the range of 150–500 ns.

The Mims ENDOR spectrum recorded at g_y orientation (maximum of EPR signal) is most resolved. Six ENDOR line pairs are clearly visible, the innermost being better visible when using longer $\tau = 500$ ns value (Fig. 2B, narrow black spectrum). Two weakly coupled ^{15}N nuclei (labeled **1** and **2** in Fig. 2B) are observed with hfc smaller than 1 MHz. These lines are highly isotropic as they demonstrate only a minor shift when recorded at g_X, g_Y, and g_Z positions. Hfc for these positions are: for line **1**—0.30 MHz, 0.27 MHz, 0.26 MHz, ($A_{iso} = 0.28$ MHz ± 0.02 MHz) for line **2**—0.69 MHz, 0.68 MHz, 0.72 MHz ($A_{iso} = 0.70$ MHz ± 0.02 MHz) correspondingly. Four additional ENDOR line pairs from stronger coupled ^{15}N nuclei are clearly observed at g_y orientation with hfcs for line **3**—1.78 MHz, line **4**—2.04 MHz, line **5**—2.26 MHz, and line **6**—2.39 MHz.

Our data does not permit the complete orientational dependence of these four ENDOR line pairs to be followed, but does allow estimation of the anisotropy range of these ^{15}N hfc tensors. We define anisotropy parameter, A_{aniso}, as a maximum difference in positions of the lines for all three canonical orientations. Thus, for line **3** the maximum shift A_{aniso} is not more than 0.2 MHz, for line **4**—$A_{aniso} < 0.2$ MHz, and for line **5**—$A_{aniso} < 0.4$ MHz, and for line **6**—$A_{aniso} < 0.4$ MHz.

In principle, up to 10 nitrogen hyperfine tensors could be observed (excluding distant nitrogens which could potentially produce a matrix-type ENDOR signal). Four pyrrole nitrogen atoms are part of each of the two Chls (P_A and P_B) comprising the primary donor P_{700}. In addition, each Chl has a histidine residue as axial ligand, which coordinates the central Mg^{2+} ion of the Chl via a nitrogen atom (Fig. 1B). However, very weakly coupled nitrogen nuclei ($|A| < 0.25$ MHz) will not be observed due to the central ENDOR hole. While strong ^{15}N hfc of up to ≈5 MHz were reported previously for P_{700}^+ [29, 65–68], we were not able to detect any lines with hfc larger than 3 MHz even by varying τ-time in a wide range 150–500 ns to eliminate the blind spot dependence. Note that these strong hfcs were obtained in ESEEM and HYSCORE experiments as parallel components $A_\parallel$ of highly anisotropic hfc

tensors. Highly anisotropic ^{15}N hyperfine couplings in general, and their parallel component particular, are difficult to detect with ENDOR spectroscopy. This might be a reason we were not able to observe these hfc lines. Alternatively, the experimental data from previous studies at lower magnetic fields with its many signals in a narrow frequency range might have been misinterpreted or incorrectly assigned.

In general, our HF data are in good agreement with ^{15}N ENDOR [29,66,69] spectroscopic results obtained at lower magnetic fields. The most significant discrepancy is found for the estimation of hfc anisotropy when compared to ESEEM and HYSCORE results. However, the direct comparison of reported data on nitrogen hfc parameters of P_{700}^{+} must be taken with care as data were reported for different PSI species, with each species potentially having slightly different protein environments surrounding the primary donor which could influence hfcs. Indeed, a certain degree of species dependence of hfc in P_{700}^{+} is observed for ^{1}H hfcs [29,30,70–72].

The main problem of data analysis is the lack of the direct assignment of hfcs to a particular nitrogen atom. Orientational dependence of ENDOR spectra does not help much as hyperfine tensor axes and g-tensor axes are not collinear and even at 130 GHz the g-tensor anisotropy is too small to allow ENDOR spectra to be recorded at a larger number of field positions (see discussion above about mw pulse excitation width vs EPR linewidth). There are several plausible assignments based on different assumptions. We assign isotropic line **2** ($A_{iso} = 0.70$ MHz) to axial N-ligand ($H660_{PsaB}$) to the Mg^{2+} of P_B, based on direct evidence from selective ^{15}N isotope labeling experiment [69]. Following this assignment, we are making the plausible assignment of isotropic line **1** ($A_{iso} = 0.28$ MHz) to the axial N-ligand ($H680_{PsaA}$) to Mg^{2+} of P_A. From this we estimate the asymmetry parameter of the spin density distribution between P_B and P_A, $R_{A/B}$ as $0.70/0.28 = 2.5$ since both histidine nitrogens are at the same distance from the Mg^{2+} ion of their respective Chl. This is in good agreement with theoretical and experimental estimations of reported spin density asymmetry parameters [29,30,62,68,70–73].

However, different assignments of line **2** were also proposed [68]. We believe that to definitely solve the assignment problem, a comprehensive study of hfc for the same species in a multifrequency ENDOR/ESEEM/HYSCORE approach with global data analysis—to eliminate the large number of adjustable parameters—is absolutely necessary. TRIPLE resonance techniques (Electron–Nuclear–Nuclear Triple Resonance) could also substantially contribute to the solution [51–53]. One-dimensional TRIPLE experiments, either heteronuclear or homonuclear would help to determine the relative signs of hfcs. Though very challenging, two-dimensional TRIPLE experiments could provide a wealth of information about the hfcs including the respective orientation of the hfc principal axes [45,74].

3.2 Electronic Structure of the Anion Radical of the Secondary Acceptor A_1^-

One way to study the secondary electron acceptor A_1^- anion radical in the A-branch is as a component of the transient radical pair $P_{700}^{+}A_{1A}^{-}$. In native PSI (no protein subunit removal and/or strongly reducing conditions), at cryogenic temperatures light-induced charge separation stops at A_1, and recombines with a halftime

of 150–200 µs, for about half the population of PSI RCs [20,75]. While the non-Boltzmann spin polarization provides a relatively strong EPR signal, the long time (≈200 µs) required to perform the ENDOR experiments on nitrogen with respect to charge recombination time and the low repetition rate of the experiment (limited by typical Laser repetition rates around 10 Hz) make it extremely challenging to perform. The alternative approach is to study the stable A_1^- anion radical, generated by reduction and the so-called photoaccumulation procedure. Incubation of PSI with sodium hydrosulfite leads to reduction of the [4Fe–4S] clusters F_A and F_B, and subsequent illumination in the 200–240 K range leads to the reduction of F_X and A_{1A}; prolonged illumination results in further reduction processes [20,25–28,39,40,45,46,76]. The photoacccumlation procedure can generate several radicals which severely spectrally overlap at standard EPR frequencies, which is problematic for the determination of magnetic resonance parameters of A_{1A}^-. Furthermore, the overlap makes it difficult to find the optimal time to stop illumination (and thus the photoaccumulation procedure). These problems can largely be prevented using high-frequency EPR with its high spectral resolution. A typical field-swept echo detected EPR spectrum at high-frequency D-band (130 GHz, 4.6 T) of dark-adapted, pre-reduced PSI recorded before illumination is shown in Fig. 3 (black spectrum). In this EPR spectrum, a background signal is seen in the range from 4.635–4.638 T (see Fig. 2A). While the position of this signal is close to P_{700}^+, the symmetry and g-tensor parameters are definitely different (compare with Fig. 2 and see Table 1). A signal from primary donor P_{700}^+ is also not expected in sodium hydrosulfite treated samples. Moreover, this signal does not change upon illumination. The origin of this background signal is not entirely clear. It might be

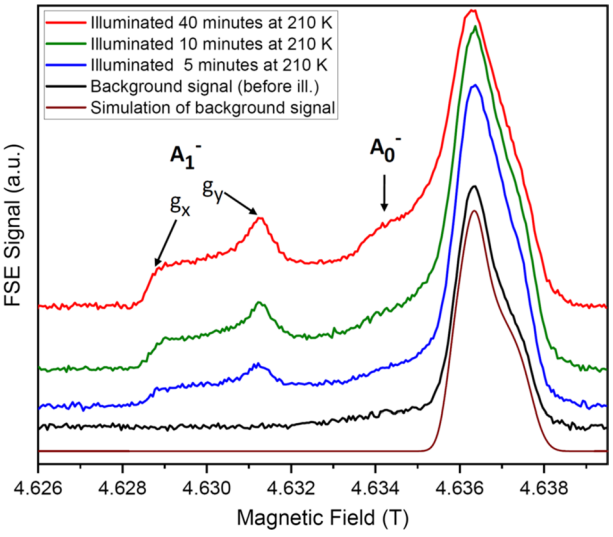

Fig. 3 High-frequency (130 GHz) pulsed EPR spectra of PSI during the photoaccumulation procedure. All spectra were recorded at $T = 210$ K. After illumination for more than ≈30 min no further increase of the secondary acceptor A_{1A}^- radical anion signal was observed

Table 1 Simulation parameters for the EPR spectra

	g_x[a]	g_y[a]	g_z[a]
P_{700}^+	2.00309	2.00263	2.00225
A_{1A}^-	2.00613	2.00496	2.00211
A_0^-	2.00393	2.00278	2.00201
SO_2^-	2.0094	2.0054	2.0018
Background	2.00301	2.00274	2.00215

[a]Relative error is ± 0.00005, while the absolute error is about twice as large. This hold only for principal components not severely overlapping with other signals where the error can be significantly higher

from some reduced Chl species, which could be part of the intrinsic light-harvesting antenna of PSI as a stress response to growth in $D_2O/^{15}N$ media, residual phycobilisome in the preparation in the detergent-containing buffer. These Chls may have undergone some chemical degradation, since Chls not shielded by the protein are quite reactive.

Within the first few minutes of illumination at 210 K the characteristic signal of A_{1A}^- begins to appear (see Fig. 3, blue and green spectra). The g_x- and g_y-components of the rhombic g-tensor of A_{1A}^- are clearly resolved and well separated from the background signal in the range from 4.635 to 4.638 T. The g_z-component of A_{1A}^- corresponds to a magnetic field of 4.638 T and is not visible due to the severe overlap with the background signal in this range. Longer illumination results in further increase of the photoaccumulated A_{1A}^- signal and appearance of additional signal at 4.634 T (Fig. 3, green and red spectra). This is due to the low field part ($\approx g_x$-component) of A_0^- [25, 27]. After approximately 30 min of illumination, no further increase of photoaccumulated A_{1A}^- signal is observed. Afterward, illumination was ceased and the sample was cooled to $T = 20$ K. At this temperature and without illumination, no further redox reactions take place and the sample is stable at least for 2 days. A field-swept echo detected EPR spectrum of this sample is shown in Fig. 4A. No major changes in lineshape are observed in the field region above 4.628 T when comparing the spectra recorded at $T = 210$ K, though the repetition rate of 25 Hz employed (optimized for detection of A_1^-) leads to some distortion of the signals above 4.634 T. In contrast, a new broad signal at magnetic fields above 4.620 T appears. This corresponds to a very large g value, not typical for organic radicals. The decomposition of the low temperature EPR spectrum into the individual components and their simulation provides the g-tensor for this species: 2.0094, 2.0054, and 2.0018 (Table 1). These parameters are in excellent agreement with those observed for sulfur dioxide anion radicals in biological samples treated with sodium dithionite [77, 78]. As expected, its relaxation times are much shorter than those of all the organic radicals, and this explains why it could not be observed by pulse EPR at $T = 210$ K where the photoaccumulation procedure was performed (Fig. 3). The other signals were simulated with the parameters listed in Table 1. The g-tensor of A_{1A}^- is in good agreement with previous high-frequency EPR measurements on frozen solutions and single crystals [25–27, 42, 58, 59, 79]. The accuracy for

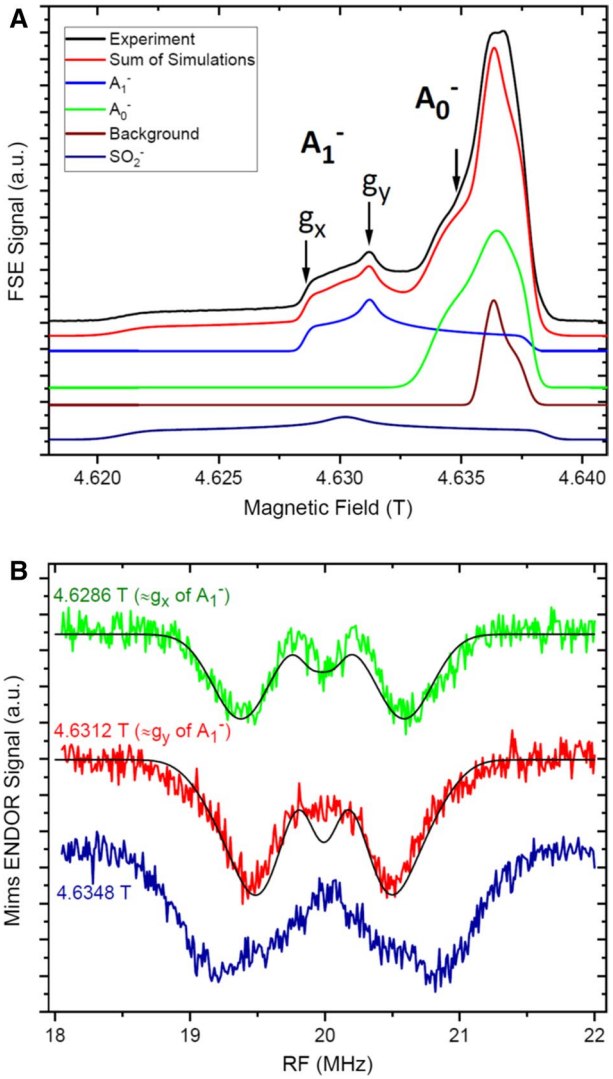

Fig. 4 High-frequency (130 GHz) pulsed EPR and ENDOR spectra of the photoaccumulated PSI. All spectra were recorded at $T=20$ K. **A** High-frequency (130 GHz, D-band) pulsed EPR spectrum of the photoaccumulated PSI (black) and its simulation (Sum of simulations in red). Arrows indicate the magnetic field positions where the ENDOR spectra were acquired. **B** ^{15}N Mims ENDOR spectra recorded at three magnetic field positions corresponding approximately to two principal values of the electronic g-tensor of A_1^- (green, red) and A_0^- (blue) Spectra were recorded with $\tau=250$ ns. Simulations of the two visible coupled ^{15}N nuclei in A_1^- (solid black lines) (color figure online)

A_0^- g-tensor is quite low since it substantially overlaps with other signals in this spectral region, but is similar to previous results [25, 27]. No hyperfine structure is visible for any of the individual species due to the large line width at D-band combined with small hyperfine coupling constants, e.g., due to the exchange of

protons by deuterons in PSI. Determination of the hyperfine coupling parameters thus requires more sophisticated techniques to resolve those interactions; in this work, we use ^{15}N Mims ENDOR as we did for P_{700}^{+}.

The ^{15}N Mims ENDOR spectra of A_{1A}^{-} were recorded at field positions corresponding to g_x and g_y orientation of the A_{1A}^{-} g-tensor (Fig. 4). The g-tensor axes from quinones like A_{1A}^{-} are in very good approximation collinear to the molecular axes, with g_x being collinear to the O–O axis, g_z being collinear to the normal of the quinone plane, and g_y orientation perpendicular to both of them [37,45,58,59,80,81]. The Chl-based radicals do not show resonance in this magnetic field range (see Fig. 4A). However, there is an overlap with the spectrum of the SO_2^{-} anion radical. But SO_2^{-} contains no magnetic nuclei which could appear in the ENDOR spectrum in the observed range. Furthermore, ^{15}N ENDOR experiments at magnetic fields lower than A_{1A}^{-} absorption did not show any signals in the spectral range of interest (not shown). We thus can conclude that the ENDOR signals detected are exclusively due to the photoaccumulated secondary electron acceptor A_{1A}^{-}. The ENDOR spectra show a clear signal of one coupled nitrogen at both g_x and g_y orientation, and an additional weak signal close to Larmor frequency at g_x orientation, with a width of about 0.2 MHz. The latter signal must be due to ^{15}N nucleus quite weakly coupled ($|A(^{15}N)| \leq 0.2$ MHz) to the unpaired electron spin of A_{1A}^{-}. A similar signal was observed in an ESEEM study of A_{1A}^{-} in ^{14}N and ^{15}N labeled PSI, but no analysis of this signal was performed by the authors of that study [43]. A hfc of 0.2 MHz for ^{15}N provides a distance from the unpaired electron of about 3.5 Å within a simple point-dipolar model, which fits well to the indole nitrogen of the tryptophan with a distance of 3.0–3.5 Å to the quinone in the PSI crystal structure [8]. This assignment of hfc to the indole nitrogen is also supported by DFT calculations of a large model of the A_1 binding site, including five surrounding amino acids [82]. All other nitrogen atoms in the crystal structure are further away and exhibit much weaker hyperfine couplings [8,82].

The more intense signal with the larger hfc is clearly due to a ^{15}N nucleus with a moderately anisotropic hyperfine tensor. The signal is also quite broad, even at the single-crystal like orientation around g_x (4.6286 T). It is not much different in overall width to the spectrum recorded at g_y (4.6312 T). This indicates that the principal axes of the hyperfine tensor are significantly deviating from the principal axes of the g-tensor (not collinear). Measurements at or close to g_z (4.636–4.638 T) are not feasible due to the strong overlap of EPR signals from different species generated during photoaccumulation (like A_0^{-}) and lower intensity of A_{1A}^{-} signals at higher fields. While we performed a spectral simulation of the two ENDOR spectra, a significant uncertainty remains due to the broad ENDOR lines observed, in particular with respect to the relative orientation of ^{15}N hyperfine tensor and g-tensor. To restrict the parameters space we assumed that the ^{15}N hyperfine tensor has an axial symmetry. Principal components of the ^{15}N hyperfine tensor are $+1.77, +0.8, +0.8$ MHz ($A_{iso} = 1.1$ MHz). These values are in good agreement with those measured for ^{14}N nuclei by HYSCORE and ESEEM techniques after scaling for the different gyromagnetic ratios of ^{15}N and ^{14}N [43, 44]. Furthermore, the DFT calculations of a large model of the A_1 binding site mentioned above, also reported an almost axial nitrogen hyperfine tensor with hfc of the same magnitude

and anisotropy, though the size of the isotropic contribution to the nitrogen hf tensor was overestimated [82]. The orientation of the parallel component of hyperfine tensor is somewhat close to the g_x tensor axis, but clearly not collinear. The simulation used the following Euler angles for the rotation of the hyperfine tensor with respect to the g-tensor: 0, 40, 30 degrees (EasySpin definition). The crystal structure of PSI shows only one other close nitrogen beside the tryptophan residue discussed above, the leucine peptide nitrogen, whose hydrogen is H-bonded to one of the oxygens of the phylloquinone (Fig. 1C). In the crystal structure, the nitrogen atom is generally along the quinone O–O axis, but has a substantial out-of-plane component and further rotation within the quinone plane [8]. In the DFT geometry optimization of a large model of the A_1 binding site where the phylloquinone is negatively charged, the orientation of the nitrogen atom has not significantly changed [82]. Taking all the evidence together, this allows us to assign with confidence this prominent ^{15}N ENDOR signal to the leucine $L722_{PsaA}$ nitrogen atom hydrogen bonded to one of the oxygen atoms of the phylloquinone anion (2.7 Å distance of leucine N to O of phylloquinone in the crystal structure). A ^{15}N ENDOR spectrum recorded at higher field (4.6348 T) is shown in Fig. 4B (blue spectrum). In this particular field position, the ENDOR spectrum is essentially an equal mixture of A_0^- and A_1^-. The spectrum is quite similar to the ENDOR spectrum recorded for A_1^-. Comparison of this spectrum with ^{15}N ENDOR of A_1^- and P_{700}^+ leads us to two conclusions. First, there are no ^{15}N hfc of A_0^- visible larger than 2 MHz. Second, the hfc of A_0^- are in the same range as hfc in coupled Chl dimer of P_{700}^+.

4 Conclusions

Here, we use D-band EPR and ENDOR spectroscopy to study the primary electron donor P_{700} and the secondary electron acceptor A_1 in Photosystem I (PSI), one of the two photosystems found in the oxygenic photosynthetic apparatus of plants and cyanobacteria. The spectra of organic cofactor radicals typically overlap severely at conventional EPR frequency of 9.5 GHz (X-band). An additional challenge is that the spectra of the individual radicals are not fully resolved at X-band. Both of these serious problems can be overcome by utilizing high-frequency (130 GHz, D-band) EPR, which provides much higher spectral resolution. Orientation-selective Electron–Nuclear-Double-Resonance spectroscopy (ENDOR) at D-band allows the determination of unresolved hyperfine interactions with magnetic nuclei, thus providing further details about the electronic properties in the protein-embedded cofactors. For this study, PSI reaction centers from cyanobacterium *Synechococcus lividus* were isotopically labeled with ^2H and ^{15}N. Deuteration of the sample decreases the inhomogeneous broadening of EPR lines, thus further improving g-tensor resolution, while ^{15}N labeling removes quadrupole interactions and significantly simplifies analysis of ENDOR spectra. Six prominent ENDOR line pairs were detected in ENDOR spectrum of P_{700}^+ which corresponds to six nitrogen nuclei coupled to the unpaired electron spin in P_{700}^+. Plausible assignment of two weak isotropic hyperfine couplings to two histidine nitrogen atoms axially ligating P_A and P_B allows estimation of the asymmetry of the spin density distribution between two chlorophylls

comprising primary electron donor P_{700}, as $R_{B/A} = 2.5$, which is in good agreement with reported data [29,30,62,70–72]. The ENDOR data on the secondary electron acceptor A_1^- allow the identification of two nitrogen atoms. One is very weakly coupled and assigned to the indole nitrogen of the tryptophan π-stacked to the phylloquinone with a distance of 3.0–3.5 Å to the quinone plane. A second more prominent nitrogen ENDOR signal could confidently be assigned to the leucine $L722_{PsaA}$ nitrogen atom H-bonded to the oxygen O_4 of the phylloquinone anion with the N–O distance of 2.7 Å in the crystal structure.

Unfortunately, our research did not elucidate the large spread of the reported experimental data. We realize that further experiments with acquiring ENDOR spectra at more field positions and with narrow excitation bandwidth might provide more information, thus improving assignment of ENDOR lines. However, these experiments will require unreasonable amount of time and resources without obvious outcome.

It is worth mentioning the definitive assignment of hfcs to specific nitrogen atoms within P_{700}^+ is too complicated even with the improved data from high-frequency ENDOR since hfc- and g-tensor axes are not collinear and available DFT and semiempirical data do not uniquely relate to experimental data. Both these factors substantially complicate analysis of orientational dependence of the ENDOR spectra.

We believe that the large spread of the EPR/ENDOR data reported for PSI is due mainly to the difference in protein isolation and handling as well as variation in the photosynthetic biological species. To achieve a definitive assignment of nitrogen hfc for these PSI cofactors, a comprehensive multifrequency ENDOR/ESEEM/HYSCORE/TRIPLE study on the same species with the same preparation technique in combination with global data analysis is absolutely necessary.

Acknowledgements The authors gratefully acknowledge support by the U.S. Department of Energy, Office of Science, Office of Basic Energy Sciences, Division of Chemical Sciences, Geosciences, and Biosciences, through Argonne National Laboratory under Contract No. DE-AC02-06CH11357. The authors acknowledge Arlene Wagner for growth of perdeuterated and ^{15}N-labeled cyanobacteria.

References

1. R.E. Blankenship, *Molecular Mechanisms of Photosynthesis* (Blackwell Science Limited, Oxford, 2002)
2. D.W. Lawlor, *Photosynthesis* (BIOS Scientific Publishers Limited, New York, 2001)
3. D. Shevela, L.O. Björn, Govindjee, *Photosynthesis: Solar Energy for Life* (World Scientific Publishing, Singapore, 2019)
4. R.E. Blankenship et al., Comparing photosynthetic and photovoltaic efficiencies and recognizing the potential for improvement. Science **332**, 805–809 (2011)
5. T.J. Wydrzynski, K. Satoh, *Photosystem II - the Light-Driven Water: Plastoquinone Oxidoreductase*, vol. 22 (Springer, Dordrecht, 2005)
6. J.H. Golbeck, *Photosystem I: The Light-Driven Plastocyanin: Ferredoxin Oxidoreductase*, vol. 24 (Springer, Dordrecht, 2006)
7. A.J. Hoff, J. Deisenhofer, Photophysics of photosynthesis. Structure and spectroscopy of reaction centers of purple bacteria. Phys. Rep. **287**, 1–247 (1997)
8. P. Jordan, P. Fromme, H.T. Witt, O. Klukas, W. Saenger, N. Krauss, Three-dimensional structure of cyanobacterial photosystem I at 2.5 Å resolution. Nature **411**, 909–917 (2001)

9. P. Fromme, P. Jordan, N. Krauss, Structure of photosystem I. Biochim. Biophys. Acta-Bioenerg. **1507**, 5–31 (2001)
10. U. Ermler, G. Fritzsch, S.K. Buchanan, H. Michel, Structure of the photosynthetic reaction center from *Rhodobacter sphaeroides* at 2.65 Å resolution—cofactors and protein–cofactor interactions. Structure **2**, 925–936 (1994)
11. M.H.B. Stowell, T.M. McPhillips, D.C. Rees, S.M. Soltis, E. Abresch, G. Feher, Light-induced structural changes in photosynthetic reaction center: implications for mechanism of electron-proton transfer. Science **276**, 812–816 (1997)
12. A. Zouni, H.T. Witt, J. Kern, P. Fromme, N. Krauss, W. Saenger, P. Orth, Crystal structure of photosystem II from *Synechococcus elongatus* at 3.8 Ångstrom resolution. Nature **409**, 739–743 (2001)
13. Y. Umena, K. Kawakami, J.R. Shen, N. Kamiya, Crystal structure of oxygen-evolving photosystem II at a resolution of 1.9 Ångstrom. Nature **473**, 55-U65 (2011)
14. M. Suga et al., Native structure of photosystem II at 1.95 Ångstrom resolution viewed by femtosecond X-ray pulses. Nature **517**, 99-U265 (2015)
15. M.G. Müller, C. Slavov, R. Luthra, K.E. Redding, A.R. Holzwarth, Independent Initiation of primary electron transfer in the two branches of the photosystem I reaction center. Proc. Natl. Acad. Sci. USA **107**, 4123–4128 (2010)
16. A.R. Holzwarth, M.G. Müller, J. Niklas, W. Lubitz, Ultrafast transient absorption studies on photosystem I reaction centers from *Chlamydomonas reinhardtii* 2: mutations near the P_{700} reaction center chlorophylls provide new insight into the nature of the primary electron donor. Biophys. J. **90**, 552–565 (2006)
17. A.R. Holzwarth, M.G. Müller, J. Niklas, W. Lubitz, Charge recombination fluorescence in photosystem I reaction centers from *Chlamydomonas reinhardtii*. J. Phys. Chem. B **109**, 5903–5911 (2005)
18. M.G. Müller, J. Niklas, W. Lubitz, A.R. Holzwarth, Ultrafast transient absorption studies on photosystem I reaction centers from *Chlamydomonas reinhardtii*. 1. A new interpretation of the energy trapping and early electron transfer steps in photosystem I. Biophys. J. **85**, 3899–3922 (2003)
19. K. Brettel, Electron transfer and arrangement of the redox cofactors in photosystem I. Biochim. Biophys. Acta-Bioenerg. **1318**, 322–373 (1997)
20. N. Srinivasan, J.H. Golbeck, Protein–cofactor interactions in bioenergetic complexes: the role of the A_{1A} and A_{1B} phylloquinones in photosystem I. Biochim. Biophys. Acta-Bioenerg. **1787**, 1057–1088 (2009)
21. J.A. Bautista, F. Rappaport, M. Guergova-Kuras, R.O. Cohen, J.H. Golbeck, J.Y. Wang, D. Beal, B.A. Diner, Biochemical and biophysical characterization of photosystem I from phytoene desaturase and Xi-carotene desaturase deletion mutants of *Synechocystis* Sp. Pcc 6803. J. Biol. Chem. **280**, 20030–20041 (2005)
22. M. Guergova-Kuras, B. Boudreaux, A. Joliot, P. Joliot, K. Redding, Evidence for two active branches for electron transfer in photosystem I. Proc. Natl. Acad. Sci. USA **98**, 4437–4442 (2001)
23. P. Joliot, A. Joliot, In vivo analysis of the electron transfer within photosystem I: Are the two phylloquinones involved? Biochemistry **38**, 11130–11136 (1999)
24. N. Dashdorj, W. Xu, R.O. Cohen, J.H. Golbeck, S. Savikhin, Asymmetric electron transfer in cyanobacterial photosystem I: charge separation and secondary electron transfer dynamics of mutations near the primary electron acceptor A_0. Biophys. J. **88**, 1238–1249 (2005)
25. O.G. Poluektov, J. Niklas, L.M. Utschig, Spin-correlated radical pairs as quantum sensors of bidirectional ET mechanisms in photosystem I. J. Phys. Chem. B **123**, 7536–7544 (2019)
26. O.G. Poluektov, L.M. Utschig, Directionality of electron transfer in type I reaction center proteins: high-frequency EPR study of PSI with removed iron-sulfur centers. J. Phys. Chem. B **119**, 13771–13776 (2015)
27. O.G. Poluektov, S.V. Paschenko, L.M. Utschig, K.V. Lakshmi, M.C. Thurnauer, Bidirectional electron transfer in photosystem I: direct evidence from high-frequency time-resolved EPR spectroscopy. J. Am. Chem. Soc. **127**, 11910–11911 (2005)
28. I.R. Vassiliev, M.L. Antonkine, J.H. Golbeck, Iron-sulfur clusters in type I reaction centers. Biochim. Biophys. Acta-Bioenerg. **1507**, 139–160 (2001)
29. A.N. Webber, W. Lubitz, P_{700}: the primary electron donor of photosystem I. Biochim. Biophys. Acta **1507**, 61–79 (2001)
30. W. Lubitz, EPR studies of the primary electron donor P_{700} in Photosystem I, in *Photosystem I: The Light-Driven Plastocyanin:Ferredoxin Oxidoreductase*. ed. by J.H. Golbeck (Springer, Dordrecht, 2006), pp. 245–269

31. K. Möbius, W. Lubitz, N. Cox, A. Savitsky, Biomolecular EPR meets NMR at high magnetic fields. Magnetochemistry **4**, 85 (2018)
32. M.C. Thurnauer, O.G. Poluektov, G. Kothe, Time-resolved high-frequency and multifrequency EPR studies of spin-correlated radical pairs in photosynthetic reaction center proteins, in *Very high frequency (Vhf) ESR/EPR*, vol. 22, ed. by O. Grinberg, L.J. Berliner (Springer, New York, 2004), pp. 166–206
33. O.G. Poluektov, L.M. Utschig, S.L. Schlesselman, K.V. Lakshmi, G.W. Brudvig, G. Kothe, M.C. Thurnauer, Electronic structure of the P_{700} special pair from high-frequency electron paramagnetic resonance spectroscopy. J. Phys. Chem. B **106**, 8911–8916 (2002)
34. K. Möbius, A. Savitsky, *High-Field EPR Spectroscopy on Proteins and Their Model Systems: Characterization of Transient Paramagnetic States* (The Royal Society of Chemistry, Cambridge, 2009)
35. P.J. Bratt, O.G. Poluektov, M.C. Thurnauer, J. Krzystek, L.C. Brunel, J. Schrier, Y.W. Hsiao, M. Zerner, A. Angerhofer, The G-factor anisotropy of plant chlorophyll A. J. Phys. Chem. B **104**, 6973–6977 (2000)
36. A. van der Est, T. Prisner, R. Bittl, P. Fromme, W. Lubitz, K. Mobius, D. Stehlik, Time-resolved X-, K-, and W-band EPR of the radical pair state $P_{700}^{\bullet+}A_1^{\bullet-}$ of photosystem I in comparison with $P_{865}^{\bullet+}Q_a^{\bullet-}$ in bacterial reaction centers. J. Phys. Chem. B **101**, 1437–1443 (1997)
37. O. Burghaus, M. Plato, M. Rohrer, K. Möbius, F. Macmillan, W. Lubitz, 3 mm high-field EPR on semiquinone radical anions $Q^{\bullet-}$ related to photosynthesis and on the primary donor $P^{\bullet+}$ and acceptor $Q_a^{\bullet-}$ in reaction centers of *Rhodobacter sphaeroides* R-26. J. Phys. Chem. **97**, 7639–7647 (1993)
38. R. Klette, J.T. Torring, M. Plato, K. Möbius, B. Bonigk, W. Lubitz, Determination of the G-tensor of the primary donor cation radical in single-crystals of *Rhodobacter sphaeroides* R-26 reaction centers by 3 mm high-field EPR. J. Phys. Chem. **97**, 2015–2020 (1993)
39. J. Bonnerjea, M.C.W. Evans, Identification of multiple components in the intermediary electron carrier complex of photosystem I. FEBS Lett. **148**, 313–316 (1982)
40. P. Gast, T. Swarthoff, F.C.R. Ebskamp, A.J. Hoff, Evidence for a new early acceptor in photosystem-I of plants—an electron-spin-resonance investigation of reaction center triplet yield and of the reduced intermediary acceptors. Biochim. Biophys. Acta **722**, 163–175 (1983)
41. S.E.J. Rigby, M.C.W. Evans, P. Heathcote, ENDOR and special triple resonance spectroscopy of $A_1^{\bullet-}$ of photosystem. Biochemistry **35**, 6651–6656 (1996)
42. F. MacMillan, J. Hanley, L. van der Weerd, M. Knupling, S. Un, A.W. Rutherford, Orientation of the phylloquinone electron acceptor anion radical in photosystem I. Biochemistry **36**, 9297–9303 (1997)
43. J. Hanley, Y. Deligiannakis, F. MacMillan, H. Bottin, A.W. Rutherford, ESEEM study of the phyllosemiquinone radical $A_1^{\bullet-}$ in ^{14}N- and ^{15}N-labeled photosystem I. Biochemistry **36**, 11543–11549 (1997)
44. N. Srinivasan, R. Chatterjee, S. Milikisiyants, J.H. Golbeck, K.V. Lakshmi, Effect of hydrogen bond strength on the redox properties of phylloquinones: a two-dimensional hyperfine sublevel correlation spectroscopy study of photosystem I. Biochemistry **50**, 3495–3501 (2011)
45. J. Niklas, B. Epel, M.L. Antonkine, S. Sinnecker, M.E. Pandelia, W. Lubitz, Electronic structure of the quinone radical anion $A_1^{\bullet-}$ of photosystem I investigated by advanced pulse EPR and ENDOR techniques. J. Phys. Chem. B **113**, 10367–10379 (2009)
46. J. Niklas, O. Gopta, B. Epel, W. Lubitz, M.L. Antonkine, Investigation of the stationary and transient $A_1^{\bullet-}$ radical in Trp -> Phe mutants of photosystem I. Appl. Magn. Reson. **38**, 187–203 (2010)
47. H.F. Daboll, H.L. Crespi, J.J. Katz, Mass cultivation of algae in pure heavy water. Biotechnol. Bioeng. **4**, 281–297 (1962)
48. L.M. Utschig, L.X. Chen, O.G. Poluektov, Discovery of native metal ion sites located on the ferredoxin docking side of photosystem I. Biochemistry **47**, 3671–3676 (2008)
49. A.Y. Bresgunov, A.A. Dubinskii, V.N. Krimov, Y.G. Petrov, O.G. Poluektov, Y.S. Lebedev, Pulsed EPR in 2-mm band. Appl. Magn. Reson. **2**, 715–728 (1991)
50. W.B. Mims, Pulsed endor experiments. Proc. R. Soc. A **283**, 452–457 (1965)
51. D. Goldfarb, S. Stoll, *EPR Spectroscopy: Fundamentals and Methods* (Wiley, New Jersey, 2018)
52. C. Gemperle, A. Schweiger, Pulsed electron-nuclear double resonance methodology. Chem. Rev. **91**, 1481–1505 (1991)
53. A. Schweiger, G. Jeschke, *Principles of Pulse Electron Paramagnetic Resonance* (Oxford University Press, New York, 2001)
54. S. Stoll, A. Schweiger, EasySpin, a comprehensive software package for spectral simulation and analysis in EPR. J. Magn. Reson. **178**, 42–55 (2006)

55. P.J. Bratt, M. Rohrer, J. Krzystek, M.C.W. Evans, L.C. Brunel, A. Angerhofer, Submillimeter high-field EPR studies of the primary donor in plant photosystem I P_{700}^{+}. J. Phys. Chem. **101**, 9686–9689 (1997)
56. A. Petrenko, A.L. Maniero, J. van Tol, F. MacMillan, Y. Li, L.C. Brunel, K. Redding, A High-field EPR study of P_{700}^{+} in wild-type and mutant photosystem I from *Chlamydomonas reinhardtii*. Biochemistry **43**, 1781–1786 (2004)
57. T.F. Prisner, A.E. McDermott, S. Un, J.R. Norris, M.C. Thurnauer, R.G. Griffin, Measurement of the g-tensor of the $P_{700}^{+\cdot}$ signal from deuterated cyanobacterial photosystem I particles. Proc. Natl. Acad. Sci. USA **90**, 9485–9488 (1993)
58. S.G. Zech, W. Hofbauer, A. Kamlowski, P. Fromme, D. Stehlik, W. Lubitz, R. Bittl, A structural model for the charge separated state $P_{700}^{\bullet+}A_1^{\bullet-}$ in photosystem I from the orientation of the magnetic interaction tensors. J. Phys. Chem. B **104**, 9728–9739 (2000)
59. C. Teutloff, W. Hofbauer, S.G. Zech, M. Stein, R. Bittl, W. Lubitz, High-frequency EPR studies on cofactor radicals in photosystem I. Appl. Magn. Reson. **21**, 363–379 (2001)
60. A.J. Stone, Gauge invariance of g-tensor. Proc. R. Soc. A **271**, 424–424 (1963)
61. A.J. Stone, g-factors of aromatic free radicals. Mol. Phys. **6**, 509–515 (1963)
62. M. Plato, N. Krauss, P. Fromme, W. Lubitz, Molecular orbital study of the primary electron donor P_{700} of photosystem I based on a recent X-ray single crystal structure analysis. Chem. Phys. **294**, 483–499 (2003)
63. R. Angstl, Contribution of the relativistic mass correction to the g-tensor of molecules. Chem. Phys. **132**, 435–442 (1989)
64. J. Telser, *Electron-Nuclear Double Resonance (ENDOR) Spectroscopy. Encyclopedia of Inorganic Chemistry* (Wiley, Chichester, 2005)
65. H. Käss, W. Lubitz, Evaluation of 2D-ESEEM data of ^{15}N-labeled radical cations of the primary donor P_{700} in photosystem I and chlorophyll a. Chem. Phys. Lett. **251**, 193–203 (1996)
66. H. Käss, E. Bittersmann-Weidlich, L.E. Andreasson, B. Bönigk, W. Lubitz, ENDOR and ESEEM of the ^{15}N labelled radical cations of chlorophyll a and the primary donor P_{700} in photosystem I. Chem. Phys. Lett. **194**, 419–432 (1995)
67. M. Mac, N.R. Bowlby, G.T. Babcock, J. McCracken, Monomeric spin density distribution in the primary donor of photosystem I as determined by electron magnetic resonance: functional and thermodynamic implications. J. Am. Chem. Soc. **120**, 13215–13223 (1998)
68. M.M. Chestnut, S. Milikisiyants, R. Chatterjee, J. Kern, A.I. Smirnov, Electronic structure of the primary electron donor $P_{700}^{+\bullet}$ in photosystem I studied by multifrequency HYSCORE spectroscopy at X- and Q-band. J. Phys. Chem. B **125**, 36–48 (2021)
69. M. Mac, X.S. Tang, B.A. Diner, J. McCracken, G.T. Babcock, Identification of histidine as an axial ligand to P_{700}^{+}. Biochemistry **35**, 13288–13293 (1996)
70. L. Krabben, E. Schlodder, R. Jordan, D. Carbonera, G. Giacometti, H. Lee, A.N. Webber, W. Lubitz, Influence of the axial ligands on the spectral properties of P_{700} of photosystem I: a study of site-directed mutants. Biochemistry **39**, 13012–13025 (2000)
71. H. Käss, P. Fromme, H.T. Witt, W. Lubitz, Orientation and electronic structure of the primary donor radical cation P_{700}^{+} in photosystem I: a single crystals EPR and ENDOR study. J. Phys. Chem. B **105**, 1225–1239 (2001)
72. H. Witt, E. Schlodder, C. Teutloff, J. Niklas, E. Bordignon, D. Carbonera, S. Kohler, A. Labahn, W. Lubitz, Hydrogen bonding to P_{700}: site-directed mutagenesis of threonine A739 of photosystem I in *Chlamydomonas reinhardtii*. Biochemistry **41**, 8557–8569 (2002)
73. D.G. Artiukhin, P. Eschenbach, J. Neugebauer, Computational investigation of the spin-density asymmetry in photosynthetic reaction center models from first principles. J. Phys. Chem. B **124**, 4873–4888 (2020)
74. D. Goldfarb, B. Epel, H. Zimmermann, G. Jeschke, 2D Triple in orientationally disordered samples—a means to resolve and determine relative orientation of hyperfine tensors. J. Magn. Reson. **168**, 75–87 (2004)
75. E. Schlodder, K. Falkenberg, M. Gergeleit, K. Brettel, Temperature dependence of forward and reverse electron transfer from A_1^{-}, the reduced secondary electron acceptor in photosystem I. Biochemistry **37**, 9466–9476 (1998)
76. M.C. Thurnauer, P. Gast, Q-band (35 GHz) electron-paramagnetic resonance results on the nature of A_1 and the electron-spin polarization in photosystem I particles. Photobiochem. Photobiophys. **9**, 29–38 (1985)

77. M.A. Yu, T. Egawa, S.R. Yeh, D.L. Rousseau, G.J. Gerfen, EPR characterization of ascorbyl and sulfur dioxide anion radicals trapped during the reaction of bovine cytochrome C oxidase with molecular oxygen. J. Magn. Reson. **203**, 213–219 (2010)
78. J. Niklas, O.G. Poluektov, High-frequency EPR of the sulfur dioxide radical—unpublished results
79. G. Link et al., Structure of the $P_{700}^{+}A_{1}^{-}$ radical pair intermediate in photosystem I by high time resolution multifrequency electron paramagnetic resonance: analysis of quantum beat oscillations. J. Am. Chem. Soc. **123**, 4211–4222 (2001)
80. B. Epel, J. Niklas, S. Sinnecker, H. Zimmermann, W. Lubitz, Phylloquinone and related radical anions studied by pulse electron nuclear double resonance spectroscopy at 34 GHz and density functional theory. J. Phys. Chem. B **110**, 11549–11560 (2006)
81. S. Sinnecker, E. Reijerse, F. Neese, W. Lubitz, Hydrogen bond geometries from electron paramagnetic resonance and electron-nuclear double resonance parameters: density functional study of quinone radical anion-solvent interactions. J. Am. Chem. Soc. **126**, 3280–3290 (2004)
82. T.J. Lin, P.J. O'Malley, Binding site influence on the electronic structure and electron paramagnetic resonance properties of the phyllosemiquinone free radical of photosystem I. J. Phys. Chem. B **115**, 9311–9319 (2011)